Suppressed deep traps and bandgap fluctuations in Cu2CdSnS4 solar cells with ≈8% efficiency

Hadke, Shreyash; Levcenko, Sergiu; Gautam, Gopalakrishnan Sai; Hages, Charles J.; Márquez, José A.; Izquierdo-Roca, Victor; Carter, Emily A.; Unold, Thomas; Wong, Lydia Helena

2019

Hadke, S., Levcenko, S., Gautam, G. S., Hages, C. J., Márquez, J. A., Izquierdo-Roca, V., ... Wong, L. H. (2019). Suppressed deep traps and bandgap fluctuations in Cu2CdSnS4 solar cells with ≈8% efficiency. Advanced Energy Materials, 9(45), 1902509-. doi:10.1002/aenm.201902509

https://hdl.handle.net/10356/146520

https://doi.org/10.1002/aenm.201902509

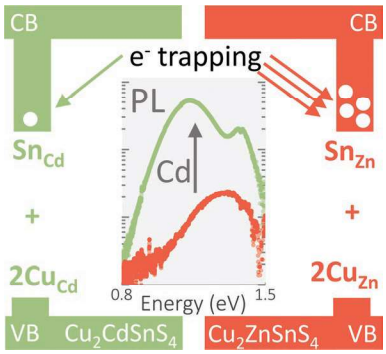

The higher photoluminescence yield and reduced bandgap fluctuations due to the substitution of Zn with Cd in Cu_2ZnSnS_4 are attributed to the suppression of deep-trap-level-inducing $2Cu_{Zn}+Sn_{Zn}$ defect cluster. The enhanced nonradiative recombination due to $2Cu_{Zn}+Sn_{Zn}$ is revealed as an important performance-limiting factor currently restricting the performance and further development of kesterite solar cells. A Cu_2CdSnS_4 solar cell with reduced bandgap fluctuations and deep traps having 7.96% efficiency is demonstrated.

ADVANCED ENERGY MATERIALS
www.advenergymat.de

Suppressed Deep Traps and Bandgap Fluctuations in Cu_2CdSnS_4 Solar Cells with ≈8% Efficiency

Shreyash Hadke, Sergiu Levcenko, Gopalakrishnan Sai Gautam, Charles J. Hages, José A. Márquez, Victor Izquierdo-Roca, Emily A. Carter, Thomas Unold, and Lydia H. Wong*

The identification of performance-limiting factors is a crucial step in the development of solar cell technologies. $Cu_2ZnSn(S,Se)_4$-based solar cells have shown promising power conversion efficiencies in recent years, but their performance remains inferior compared to other thin-film solar cells. Moreover, the fundamental material characteristics that contribute to this inferior performance are unclear. In this paper, the performance-limiting role of deep-trap-level-inducing $2Cu_{Zn}+Sn_{Zn}$ defect clusters is revealed by comparing the defect formation energies and optoelectronic characteristics of Cu_2ZnSnS_4 and Cu_2CdSnS_4. It is shown that these deleterious defect clusters can be suppressed by substituting Zn with Cd in a Cu-poor compositional region. The substitution of Zn with Cd also significantly reduces the bandgap fluctuations, despite the similarity in the formation energy of the $Cu_{Zn}+Zn_{Cu}$ and $Cu_{Cd}+Cd_{Cu}$ antisites. Detailed investigation of the Cu_2CdSnS_4 series with varying Cu/[Cd+Sn] ratios highlights the importance of Cu-poor composition, presumably via the presence of V_{Cu}, in improving the optoelectronic properties of the cation-substituted absorber. Finally, a 7.96% efficient Cu_2CdSnS_4 solar cell is demonstrated, which shows the highest efficiency among fully cation-substituted absorbers based on Cu_2ZnSnS_4.

1. Introduction

Advances in thin-film solar cells rely heavily on the identification and mitigation of performance-limiting factors. Successful examples of such advances include the introduction of postdeposition alkali treatment to improve heterojunction diode quality in Cu(In,Ga)Se_2 (CIGS) solar cells and chloride treatment to passivate grain boundaries in CdTe solar cells.[1] These solar-cell technologies are already commercialized, with lab-scale photovoltaic efficiencies exceeding 22%.[2] However, kesterite-based solar cells, such as $Cu_2ZnSn(S,Se)_4$, which share many of the same characteristics of CIGS and CdTe, significantly lag behind, with a record power conversion efficiency (PCE) of 12.6%.[3]

Although the dominant limiting factors for this low performance are a matter of considerable discussion,[4] the following observations are consistent among kesterite absorbers: i) a low photoluminescence quantum yield (PLQY) and a short charge-carrier lifetime,[5] ii) a high value of Urbach band tail energy (larger than 30 meV for S-rich kesterites) and lack of a steep absorption onset,[6,7] and iii) the presence of secondary phases.[4,6,8,9] The extent to which these factors individually affect the photovoltaic performance is debated, but their ubiquity among kesterite absorbers indicates the presence of a large density of point defects.[10–12] Specifically, i) the low PLQY arises from the presence of nonradiative mid-gap defects,[5] ii) the high value of

S. Hadke, Prof. L. H. Wong
School of Materials Science and Engineering
Nanyang Technological University
Singapore 639798, Singapore
E-mail: lydiawong@ntu.edu.sg
S. Hadke, Prof. L. H. Wong
Energy Research Institute @ NTU (ERI@N)
Nanyang Technological University
Singapore 637553, Singapore
S. Hadke
Interdisciplinary Graduate School
Nanyang Technological University
Singapore 637371, Singapore
Dr. S. Levcenko, Dr. J. A. Márquez, Dr. T. Unold
Department of Structure and Dynamics of Energy Materials
Helmholtz-Zentrum fur Materialien und Energie
Berlin 14109, Germany
The ORCID identification number(s) for the author(s) of this article can be found under https://doi.org/10.1002/aenm.201902509.

DOI: 10.1002/aenm.201902509

Dr. G. Sai Gautam
Department of Mechanical and Aerospace Engineering
Princeton University
Princeton, NJ 08544-5263, USA
Prof. C. J. Hages
Department of Chemical Engineering
University of Florida
Gainesville, FL 32611, USA
Dr. V. Izquierdo-Roca
Catalonia Institute for Energy Research (IREC)
Jardin de les Dones de Negre 1, Barcelona 08930, Spain
Prof. E. A. Carter
School of Engineering and Applied Science
Princeton University
Princeton, NJ 08544-5263, USA
Prof. L. H. Wong
Campus for Research Excellence And Technological Enterprise (CREATE)
1 Create Way, Singapore 139602, Singapore

Urbach tail energy and lack of a steep absorption onset suggests bandgap fluctuations due to compositional variations[13] and/or compensated defect clusters close to the band edges,[14] and iii) the presence of secondary phases is linked to the off-stoichiometric composition that is required to increase the formation energy of point defects.[12,15]

Several theorists have studied the possible role of point defects in Cu_2ZnSnS_4 and $Cu_2ZnSnSe_4$. The earliest reports identified the Cu_{Zn} antisite and the compensated Cu_{Zn}+Zn_{Cu} cluster as the dominant defects.[16] Further studies that considered more defects and defect clusters also corroborated this conclusion.[17] However, the partially compensated Cu_{Zn}+Sn_{Zn} and the fully compensated $2Cu_{Zn}$+Sn_{Zn} clusters were not considered in these studies. In 2012, Chen et al. reported a low formation energy for Cu_{Zn}+Sn_{Zn} and $2Cu_{Zn}$+Sn_{Zn} in kesterites and also proposed their deleterious role of introducing deep defects and bandgap narrowing.[18] Another report in 2015 concerned with deep recombination centers in $Cu_2ZnSnSe_4$ predicted a large density of Sn_{Zn} defects and suggested that this defect would significantly contribute to charge-carrier recombination.[19] Hence, based on theoretical calculations, the possible performance-limiting point defects in kesterites are proposed to be the Cu-Zn antisite Cu_{Zn}+Zn_{Cu}, and the deep-trap-level-inducing Sn-antisite $2Cu_{Zn}$+Sn_{Zn}. However, experimental evidence supporting these theoretical point defect studies is scarce.[6]

Altering the point-defect characteristics using cation substitution is reported to enhance the photovoltaic performance of kesterites, showing especially promising results for the substitution of Zn^{2+} by isovalent ions such as Ba^{2+}, Mn^{2+}, and Cd^{2+}.[6,9,11,20–23] Here, we study the role of the proposed performance-limiting defects Cu_{Zn}+Zn_{Cu} and $2Cu_{Zn}$+Sn_{Zn} by systematically substituting cations in Cu_2ZnSnS_4 as characterized by both experimental and theoretical methods. Specifically, we study the trends in experimental and theoretical results upon replacing Zn with a +2 valence cation. Among the promising +2 valence cations, we choose Cd for three main reasons.

i) Cd is expected to suppress the formation of Cu_{Cd}+Cd_{Cu} defect clusters in Cu_2CdSnS_4, which are similar to the Cu_{Zn}+Zn_{Cu} clusters in Cu_2ZnSnS_4.[15] This is because the ionic radius of tetrahedrally coordinated Cd^{2+} is 30% larger than that of Zn^{2+},[24] with the prevalence of Cu_{Zn}+Zn_{Cu} in Cu_2ZnSnS_4 often attributed to the similar ionic radii of Cu and Zn.[6,13,20,25]
ii) Cu_2ZnSnS_4 (kesterite-type structure) has Cu-Zn planes and Cu-Sn planes (Figure S1, Supporting Information) along the *c*-axis, with the Cu-Zn plane showing the highest degree of cationic disorder;[26] Cu_2CdSnS_4 (expected to be in a stannite-type structure[15]) has Cu-only and Cd-Sn planes (Figure S1, Supporting Information) along the *c*-axis, and the lack of a Cu-Cd plane may mitigate the Cu-Cd disorder.
iii) Cd is predicted to affect the formation energy of deep-trap-level-inducing $2Cu_{Zn}$+Sn_{Zn} cluster.[11]

We study the effects of Cd substitution by combining results from experimental structural and optoelectronic characterizations with point defect formation energies predicted by density functional theory (DFT). While we find similar formation energies for Cu_{Zn}+Zn_{Cu} in Cu_2ZnSnS_4 and Cu_{Cd}+Cd_{Cu} in Cu_2CdSnS_4, we observe that replacing Zn with Cd penalizes formation of the deep-electron-trapping Sn-antisite defect cluster, $2Cu_{Cd}$+Sn_{Cd}. Furthermore, we show through calculations that this effect is not related to the change of the structure from kesterite to stannite, but rather is a result of Cd substitution. We demonstrate experimentally that Cu_2CdSnS_4 films exhibit significantly larger photoluminescence (PL) yield, longer PL decay time and smaller bandgap fluctuations as compared to Cu_2ZnSnS_4 films prepared using the same deposition process. We also assess the effect of different Cu/[Cd+Sn] ratios on the optoelectronic properties of Cu_2CdSnS_4, and in doing so, demonstrate a Cu_2CdSnS_4-based device having 7.96% active area (7.85% total area) power conversion efficiency, which is the highest efficiency among fully cation-substituted absorbers based on Cu_2ZnSnS_4.

2. Results and Discussion

The differences in the defect characteristics of Cu_2ZnSnS_4 and Cu_2CdSnS_4 are studied experimentally by comparing the optoelectronic properties of Cu_2ZnSnS_4 and Cu_2CdSnS_4 at the same cation ratio, Cu/[Zn+Sn] = Cu/[Cd+Sn] = 0.86. This ratio is chosen because we obtain the best efficiency for Cu_2ZnSnS_4 at this ratio. For a more detailed characterization of the Cu_2CdSnS_4 system, we also fabricated Cu_2CdSnS_4 samples with Cu/[Cd+Sn] = 0.68, 0.74, 0.80, 0.92, and 0.98. However, at very low and high values of this ratio, we get secondary phases (see Section 2.1), and hence, only data corresponding to ratios 0.80, 0.86, and 0.92 are reported here. Consequently, the four compositions studied in detail in this paper are a) Cu_2ZnSnS_4 with Cu/[Zn+Sn] = 0.86, b) Cu_2CdSnS_4 with Cu/[Cd+Sn] = 0.86, c) Cu_2CdSnS_4 with Cu/[Cd+Sn] = 0.80, and d) Cu_2CdSnS_4 with Cu/[Cd+Sn] = 0.92. These compositions are referred to as Cu_2ZnSnS_4(0.86), Cu_2CdSnS_4(0.86), Cu_2CdSnS_4(0.80), and Cu_2CdSnS_4(0.92), respectively.

2.1. Structural Characterization

2.1.1. Crystal Structure of Cu_2ZnSnS_4 and Cu_2CdSnS_4 at Cu/[Zn+Sn] = Cu/[Cd+Sn] = 0.86

The similar atomic number (and hence the similar atomic form factor[27]) of Cu and Zn makes these elements difficult to differentiate using the conventional Cu-K_α radiation, and hence, X-ray diffraction (XRD; **Figure 1**a, solid blue line) cannot be used to confirm whether Cu_2ZnSnS_4 thin films adopt a kesterite or a stannite structure.[28] Figure 1b (solid blue line) illustrates this by comparing the XRD pattern for Cu_2ZnSnS_4(0.86) with the simulated XRD patterns for Cu_2ZnSnS_4 with a kesterite, disordered kesterite (complete disorder on 2c and 2d sites), and stannite structures. There are multiple reports showing that Cu_2ZnSnS_4 crystallizes in the kesterite type structure.[29] Moreover, the Raman spectra measured here for Cu_2ZnSnS_4(0.86) (Figure 1c, solid blue line) is consistent with the ones reported in literature for kesterite Cu_2ZnSnS_4.[30] Based on the XRD and Raman data, we infer that the Cu_2ZnSnS_4 film studied here adopts either the kesterite type structure or a (fully or partially) disordered kesterite structure.

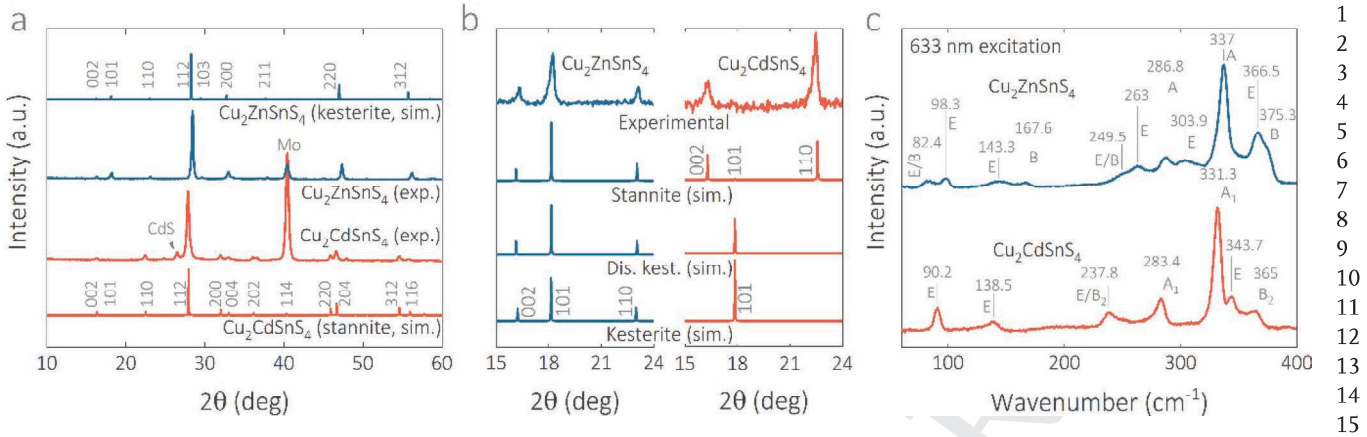

Figure 1. a,b) Experimental and simulated XRD patterns and c) Raman spectra for Cu_2ZnSnS_4 (Cu/[Zn+Sn] = 0.86) and Cu_2CdSnS_4 (Cu/[Cd+Sn] = 0.86).

The substitution of Zn with the higher atomic number Cd (and the associated difference in the atomic form factor[27]) makes the structure factor for X-rays distinct enough to reliably study Cu_2CdSnS_4 using conventional XRD analysis. Figure 1b (solid red line) illustrates this by comparing the experimental XRD pattern for Cu_2CdSnS_4(0.86) with the simulated patterns for Cu_2CdSnS_4 with stannite, disordered kesterite, and kesterite structures (detailed information in Figures S1 and S2, Supporting Information). Although we cannot ignore the texture effects associated with thin-film XRD, the experimental pattern clearly matches the simulated one for stannite Cu_2CdSnS_4 (note that the XRD peak at ≈40.5° in the experimental XRD pattern does not correspond to the 114 peak in the simulated XRD pattern for stannite Cu_2CdSnS_4 but rather to the Mo substrate). Figure S2 in the Supporting Information also shows that the observed differences in the intensity of peaks are not due to the change in the ratio of the lattice parameter c/a due to the incorporation of Cd, but rather, are a result of the change in the structure factor as Cd is incorporated in the lattice. The observation of a stannite crystal structure for Cu_2CdSnS_4 is also consistent with DFT calculations that predict stannite Cu_2CdSnS_4 as more thermodynamically stable than kesterite Cu_2CdSnS_4.[15]

2.1.2. Secondary Phases

The XRD results (Figure 1a) reveal a peak corresponding to CdS in the Cu_2CdSnS_4 thin films, which is consistent with the observation of a CdS peak in the Raman spectra of Cu_2CdSnS_4 at an excitation wavelength of 532 nm, where CdS shows resonant Raman scattering (Figure S3, Supporting Information). Under the resonant Raman scattering conditions for ZnS (325 nm excitation), the peaks for ZnS appear in the Raman spectrum of Cu_2ZnSnS_4 (Figure S3, Supporting Information). Although secondary phases form in Cu_2ZnSnS_4 and Cu_2CdSnS_4, in the partially Cd-substituted $Cu_2(Zn,Cd)SnS_4$ series (Cd/[Cd+Zn] = 0.20, 0.30, 0.40, 0.60, 0.80), neither ZnS nor CdS are observed in the Raman spectra (Figure S4, Supporting Information). This suggests that partial cation substitution might address the problem of secondary phase formation in kesterite absorbers.

2.1.3. Effect of Varying the Copper Content in Cu_2CdSnS_4

We do not observe any significant changes in either the XRD patterns or Raman spectra as Cu/[Cd+Sn] is varied from 0.80 to 0.92 (Figure S5, Supporting Information). The observation of CdS is consistent in the XRD and Raman results, and the peak corresponding to CdS does not change in intensity with the change in the Cu/[Cd+Sn] ratio within 0.80 and 0.92, suggesting that similar amount of CdS is present in these films. However, at lower Cu/[Cd+Sn] ratios (0.68 and 0.74), we observe an increase in the Raman yield for CdS; and for higher Cu/[Cd+Sn] ratio (0.98), we detect Raman peaks for Cu_xS (Figure S6, Supporting Information). Hence, in this report, we limit our analysis to Cu/[Cd+Sn] ratios of 0.80, 0.86, and 0.92, to decouple the effect of secondary phases and the Cu/[Cd+Sn] ratio.

2.2. Defect Characteristics

2.2.1. Defect Formation Energy

We calculated the formation energy of various defects and defect clusters using DFT (see the Experimental Section for details) to study the effect of Cd substitution. DFT has been used extensively to predict defects in semiconductors, with studies often reporting excellent agreement between theory and experiment.[31] All the defects and defect clusters considered in this work are neutral defects.[15,32] The calculations were performed for three structures: a) kesterite Cu_2ZnSnS_4, b) stannite Cu_2ZnSnS_4, and c) stannite Cu_2CdSnS_4. We present the results for kesterite Cu_2ZnSnS_4 and stannite Cu_2CdSnS_4 in **Figure 2** and those for stannite Cu_2ZnSnS_4 in Figure S7 in the Supporting Information.

We plot the defect formation energies as a function of copper chemical potential (μ_{Cu}) and include the following three scenarios:

i) Cu-rich (μ_{Cu} = 0 eV): Cu_2ZnSnS_4/Cu_2CdSnS_4 in equilibrium with metallic Cu, and Zn/Cd and Sn chemical potentials constrained to be in equilibrium with ZnS/CdS and SnS (Zn/Cd-rich and Sn-rich), respectively;

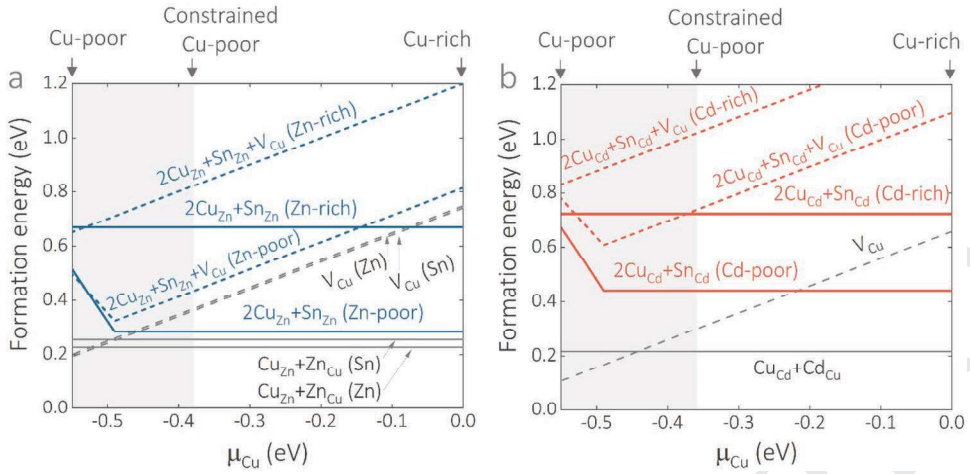

Figure 2. Formation energies of various defects and defect clusters as a function of Cu chemical potential (μ_{Cu}) in a) kesterite Cu_2ZnSnS_4 and b) stannite Cu_2CdSnS_4. In (a), the (Zn) and (Sn) notation corresponds to defects present in the Zn-plane and Sn-plane in the kesterite structure (004 and 002 planes in Figure S1, Supporting Information), respectively.

ii) Constrained Cu-poor (μ_{Cu} = −0.38 eV in Cu_2ZnSnS_4 and −0.36 eV in Cu_2CdSnS_4): The most negative Cu chemical potential that stabilizes Cu_2ZnSnS_4/Cu_2CdSnS_4 while maintaining Zn/Cd-rich and Sn-rich conditions (equilibrium with ZnS/CdS and SnS);

iii) Cu-poor (μ_{Cu} = −0.57 eV in Cu_2ZnSnS_4, −0.56 eV in Cu_2CdSnS_4): The most negative Cu chemical potential without any constraints on the chemical potentials of Zn/Cd and Sn.

Experimentally, we use a Cu-poor (Cu/[Cu+Sn+Zn] = 0.46), Sn-poor (Sn/[Cu+Sn+Zn] = 0.24), and Zn-rich (Zn/[Cu+Sn+Zn] = 0.30) composition. Hence, the experimental data correspond to the DFT results in the Cu-chemical potential range between "constrained Cu-poor" and "Cu-poor" (details in Figure S7, Supporting Information). We shade this region in gray in Figure 2a,b. Defects having a high formation energy (>1 eV for μ_{Cu} = 0 to −0.57 eV), such as $Sn_{Cu}+Cu_{Sn}$, $Sn_{Zn}+Zn_{Sn}$, and $Cd_{Sn}+Sn_{Cd}$ are not included in the figures, since their concentration at room temperature will be insignificant.

2.2.2. $Cu_{Zn}+Zn_{Cu}$ and $Cu_{Cd}+Cd_{Cu}$ Disorder

One of the reasons for the abundance of Cu-Zn disorder in Cu_2ZnSnS_4 is proposed to be the similar size of Cu^+ and Zn^{2+} cations.[6,13,20] However, the formation energy of $Cu_{Zn}+Zn_{Cu}$ antisite (solid gray line in Figure 2a) remains unaffected by the complete substitution of Zn with the larger Cd cation, i.e., the formation energy of $Cu_{Cd}+Cd_{Cu}$ in stannite-Cu_2CdSnS_4 (0.22 eV, solid gray line in Figure 2b) is similar to $Cu_{Zn}+Zn_{Cu}$ in kesterite-Cu_2ZnSnS_4 (0.22–0.25 eV, solid gray lines in Figure 2a). The similarity in the formation energies of $Cu_{Zn}+Zn_{Cu}$ and $Cu_{Cd}+Cd_{Cu}$ antisites may be attributed to the small energy difference (≈28–29 meV/f.u.) of the kesterite and stannite polymorphs in Cu_2ZnSnS_4 and Cu_2CdSnS_4.[8,10,15] The formation energy for Cu-Zn and Cu-Cd disorder caused by these antisite defects is consistent with the values reported in other theoretical studies.[11] Hence, we infer that the differences in optoelectronic properties between Cu_2ZnSnS_4 and Cu_2CdSnS_4 are not directly related to the disorder-inducing $Cu_{Zn}+Zn_{Cu}$ and $Cu_{Cd}+Cd_{Cu}$ antisites.

2.2.3. V_{Cu}, $2Cu_{Zn}+Sn_{Zn}$, and $2Cu_{Cd}+Sn_{Cd}$ Defects

There are two major differences in the defect characteristics for Cu_2ZnSnS_4 and Cu_2CdSnS_4: i) the lower formation energy for a Cu-vacancy (V_{Cu}) in Cu_2CdSnS_4 (≈0.1–0.66 eV, Figure 2b) as compared to Cu_2ZnSnS_4 (≈0.17–0.74 eV, Figure 2a) and ii) the higher formation energy of $2Cu_{Cd}+Sn_{Cd}$ in Cu_2CdSnS_4 (≈0.44–0.72 eV, Figure 2b) as compared to $2Cu_{Zn}+Sn_{Zn}$ in Cu_2ZnSnS_4 (≈0.28–0.67 eV, Figure 2a). Since V_{Cu} is a shallow defect that can potentially act as a shallow acceptor,[10] its presence in these materials is beneficial, or at worst, benign. However, the $2Cu_{Cd}+Sn_{Cd}$ and $2Cu_{Zn}+Sn_{Zn}$ clusters induce deep electron traps and can degrade the photovoltaic performance.[12] The difference in formation energies of these defect clusters is particularly larger under Cd-poor (≈0.44–0.67 eV) in comparison to Zn-poor (≈0.28–0.51 eV) conditions in Cu_2CdSnS_4 and Cu_2ZnSnS_4, respectively. Given the prevalence of composition fluctuations in Cu_2ZnSnS_4,[33] and the formation of secondary ZnS phase at the surface[23] that can make the surrounding kesterite phase relatively Zn-poor, isolated domains of these deep-trap-inducing defects in Zn- or Cd-poor domains can significantly affect the optoelectronic performance. Additionally, the formation energy of the $2Cu_{Zn}+Sn_{Zn}$ cluster is consistently lower in the stannite polymorph of Cu_2ZnSnS_4 (≈0.12–0.51 eV, Figure S7, Supporting Information) than kesterite-Cu_2ZnSnS_4 (Figure 2a). Thus, the suppression of these defect clusters in Cu_2CdSnS_4 compared to Cu_2ZnSnS_4 is related to the substitution of Zn with Cd atoms and not due to the stabilization of the stannite structure. Therefore, DFT calculations suggest that stannite Cu_2CdSnS_4 should exhibit better optoelectronic characteristics than kesterite Cu_2ZnSnS_4, primarily due to the suppression of deep electron traps.

2.2.4. Simulation of Cu-Poor Stoichiometries

Note that the terms "rich" and "poor" used in Figure 2 and Figure S7 in the Supporting Information are not representative

of the actual compositional stoichiometry of the system but rather they correspond to the endpoints in the chemical potential space that stabilize compositionally stoichiometric Cu_2ZnSnS_4/Cu_2CdSnS_4. Thus, low values of μ_{Cu} do not signify any Cu-deficiency within bulk Cu_2ZnSnS_4/Cu_2CdSnS_4, i.e., do not signify a compositionally Cu-poor condition. Instead, a low μ_{Cu} indicates a lower availability of Cu for the formation of defects that require the exchange (addition/removal) of a Cu atom. Therefore, to better simulate compositionally Cu-poor conditions (e.g., Cu/[Cd+Sn] = 0.80) used in fabricating Cu_2ZnSnS_4 solar cells, we calculated the formation energy of $2Cu_{Zn}+Sn_{Zn}$ and $2Cu_{Cd}+Sn_{Cd}$ in conjunction with V_{Cu}, i.e., the formation energy of $2Cu_{Zn}+Sn_{Zn}+V_{Cu}$ and $2Cu_{Cd}+Sn_{Cd}+V_{Cu}$. Physically, this corresponds to having a copper vacancy adjacent to a $2Cu_{Zn}+Sn_{Zn}$ or a $2Cu_{Cd}+Sn_{Cd}$ cluster. Six symmetrically distinct configurations of $2Cu_{Zn}+Sn_{Zn}+V_{Cu}$ exist in the kesterite structure, whereas four distinct configurations exist in stannite Cu_2ZnSnS_4 and Cu_2CdSnS_4, with the lowest energy configurations plotted in Figure 2 and Figure S7 in the Supporting Information.

In both Cu_2ZnSnS_4 and Cu_2CdSnS_4, the predicted formation energy of the $2Cu_{Zn}+Sn_{Zn}$ and $2Cu_{Cd}+Sn_{Cd}$ cluster is higher in the presence of V_{Cu} (≈0.32–1.2 eV in Figure 2a and ≈0.6–1.38 eV in Figure 2b and Figure S7, Supporting Information) than in its absence, i.e., Cu-deficiency suppresses formation of $2Cu_{Zn}+Sn_{Zn}$ and $2Cu_{Cd}+Sn_{Cd}$. The $2Cu_{Cd}+Sn_{Cd}$ cluster is suppressed to a larger extent in the presence of V_{Cu} in Cu_2CdSnS_4 (dashed vs solid red lines in Figure 2b) than what is found for $2Cu_{Zn}+Sn_{Zn}$ in kesterite Cu_2ZnSnS_4 (dashed vs solid blue line in Figure 2a). Note that isolated V_{Cu} tends to form more readily in Cu_2CdSnS_4 than Cu_2ZnSnS_4 (dashed gray lines in Figure 2a,b). Thus, under Cu-poor conditions (low μ_{Cu}), especially in compositionally Cu-deficient samples, Cd is more effective than Zn in suppressing these deep-defect clusters, further highlighting the beneficial role of Cd. Moreover, the similar formation energy of the $2Cu_{Zn}+Sn_{Zn}$ cluster in the presence of V_{Cu} in kesterite and stannite-Cu_2ZnSnS_4 (Figure 2a and Figure S7, Supporting Information) suggests that the suppression of the $2Cu_{Cd}+Sn_{Cd}$ clusters is due to Cd substitution, rather than due to the structural change from kesterite to stannite.

2.3. Photoluminescence and Time-Resolved Photoluminescence

2.3.1. Effect of Cd Substitution on Photoluminescence and Time-Resolved Photoluminescence Characteristics (Cu/[Zn+Sn] = Cu/[Cd+Sn] = 0.86)

The proposed suppression of the deep $2Cu_{Zn}+Sn_{Zn}$ traps should lead to a longer charge-carrier lifetime, due to the suppression of Shockley–Reed–Hall (SRH)-type recombination. This would be reflected in a higher PL yield in steady-state PL and a longer PL decay time in time-resolved PL (TRPL) measurements. Hence, these techniques can be used to validate experimentally the proposed effect of the suppression of deep $2Cu_{Zn}+Sn_{Zn}$ traps.

The room-temperature PL spectrum on Cu_2ZnSnS_4 devices (**Figure 3**a, solid blue dots) consists of a single peak around 1.3 eV, while that for Cu_2CdSnS_4 devices (Figure 3a, solid red

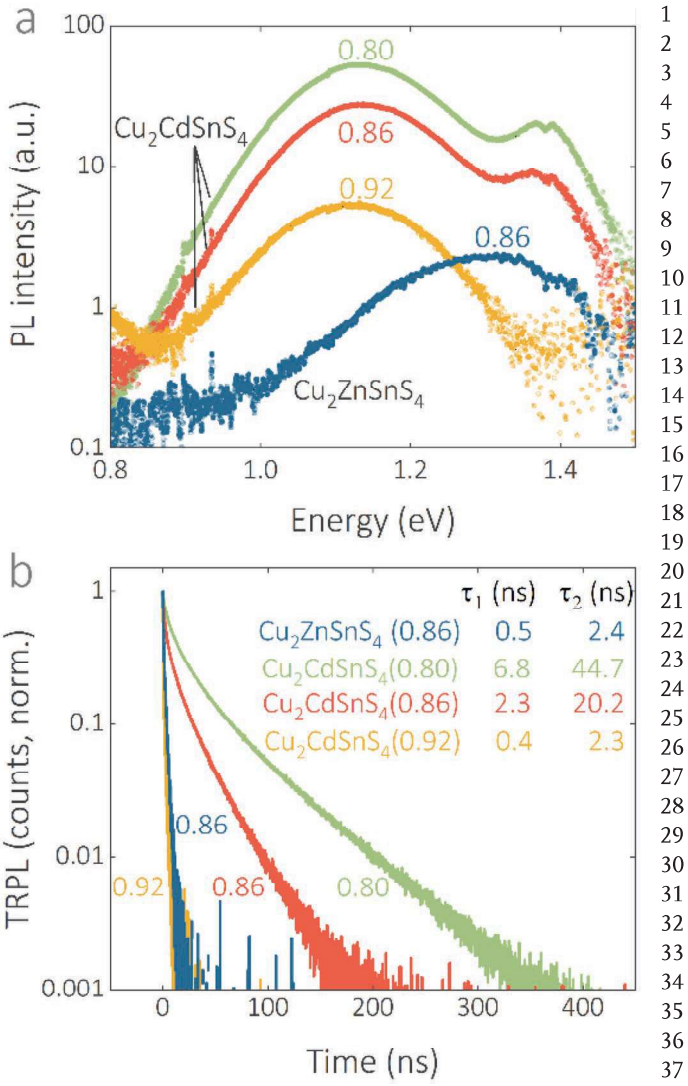

Figure 3. a) Room-temperature steady-state photoluminescence (PL) and b) time-resolved photoluminescence (TRPL). Data are shown for Cu/[Zn+Sn] = 0.86 and Cu/[Cd+Sn] = 0.80, 0.86, and 0.92. PL decay times (τ) given in the inset of (b). PL and TRPL measurements were performed using a 660 nm laser excitation.

dots) consists of two peaks at 1.14 and 1.38 eV. Based on our previous work[22] on temperature-dependent PL of Cu_2ZnSnS_4, we assign the peak around 1.3 eV to a free-to-bound (FB) transition,[34] that is, the recombination of a free electron from the conduction band with a trapped hole in acceptor defect levels near the valence band. Similarly, we assign the low-energy peak in Cu_2CdSnS_4 (1.14 eV) to a free-to-bound transition. Furthermore, based on temperature-dependent PL analysis (Figure S8a, Supporting Information), we assign the high energy peak (1.38 eV) to a band-to-band (BB) transition, consistent with the observation of a BB transition in monograin Cu_2CdSnS_4 samples.[35] Figure S8b,c in the Supporting Information shows the fitting of the PL spectra to a summation of two Gaussian curves.

The integrated PL intensity (I_{PL}) of the FB peak for Cu_2CdSnS_4 (I_{PL} = 6.1 a.u.) is more than an order of magnitude

higher than that for Cu_2ZnSnS_4 (I_{PL} = 0.52 a.u.). The FB transition intensity is proportional to i) injection level, that is, the excess carrier density due to light excitation, ii) the occupancy of the acceptor defect levels N_A, and iii) the recombination time of charge carriers. The injection level in these measurements is similar for three reasons: the charge carrier density measured using the AC-Hall technique is nearly identical for Cu_2ZnSnS_4 (2.8×10^{16} cm^{-3}) and Cu_2CdSnS_4 (2.7×10^{16} cm^{-3});[22] the thickness,[23] reflectance (Figure S9, Supporting Information), and absorption coefficient of the absorber at ≈660 nm[36] does not change with Cd substitution; and the samples are measured under the same excitation conditions. The occupied states in the acceptor defect levels are influenced by temperature—not varied in our experiment—and the donor states (N_D). Hence, under the assumptions that the acceptor/donor states are similar in these materials, the higher PL yield in Cu_2CdSnS_4 indicates that Cu_2CdSnS_4 has a longer charge-carrier lifetime than Cu_2ZnSnS_4. This interpretation is corroborated by the fact that with the increasing PL yield of the defect transition, we also observe an increasing contribution of the BB recombination around 1.38 eV, which can be considered directly proportional to the effective charge-carrier recombination time. BB transitions are rarely observed in Cu_2ZnSnS_4; such transitions are an indicator of the superior electronic quality of the Cd-based material as they imply less defects in the material.

The charge-carrier lifetime can be analyzed more directly by TRPL. The normalized TRPL data (Figure 3b) suggest a longer PL decay time for Cu_2CdSnS_4 (solid red curve) as compared to Cu_2ZnSnS_4 (solid blue curve). A biexponential fit to the PL decay curve of Cu_2CdSnS_4 reveals a PL decay time of 2.3 and 20.2 ns for the fast and slow decay regimes, while the corresponding PL decay times for Cu_2ZnSnS_4 are 0.5 and 2.4 ns, respectively. The PL decay time in semiconductors with large amounts of shallow trapping states may significantly overestimate the real minority carrier lifetime.[5] However, considering the capture and emission of carriers from shallow traps, the decay time is proportional to $\tau_N \times \tau_E/\tau_C$, where τ_N is the SRH-recombination time, τ_E is the emission time of trapped carriers, and τ_C is the capture time for carrier trapping. Thus, if the capture and emission from shallow traps are approximately constant, changes in the PL decay can be related qualitatively to changes in the true charge-carrier lifetime. The improvement in the PL decay time upon substitution of Zn with Cd as found in Figure 3b thus supports the DFT calculations that suggest a suppression of the deep Sn-related defects in Cu_2CdSnS_4.

If the increase in the PL decay time and steady-state PL yield is due to the suppression of deep defects as Zn is replaced with Cd, then the steady-state PL yield in the $Cu_2(Zn,Cd)SnS_4$ series should increase with Cd/[Cd+Zn] due to the larger formation energy of $2Cu_{Cd}+Sn_{Cd}$ in Cu_2CdSnS_4 as compared to $2Cu_{Zn}+Sn_{Zn}$ in Cu_2ZnSnS_4. Experimentally, we indeed observe a monotonic increase in the steady state PL yield with increasing Cd/[Cd+Zn] ratio (Figure S10, Supporting Information). Thus, based on theoretical and experimental results in Figures 2a,b and 3a,b, and the assumption that the shallow donor and acceptor states do not change significantly, we conclude that the lower formation energy of the deleterious $2Cu_{Zn}+Sn_{Zn}$ defect cluster compared to that of $2Cu_{Cd}+Sn_{Cd}$ is a major factor that facilitates the enhanced nonradiative recombination (and hence a shorter PL decay time) in Cu_2ZnSnS_4 as compared to Cu_2CdSnS_4.

2.3.2. Effect of Cu Content in Cu_2CdSnS_4 on PL and TRPL Characteristics

The formation energy of $2Cu_{Cd}+Sn_{Cd}$ can be altered by using copper-poor stoichiometry (Section 2.2.4). Hence, to further support the hypothesis that the $2Cu_{Cd}+Sn_{Cd}$ cluster in Cu_2CdSnS_4 contributes to nonradiative recombination, we study the effect of the Cu/[Cd+Sn] ratio on the steady-state PL and TRPL characteristics.

The PL yield increases as the Cu/[Cd+Sn] ratio decreases, while the apparent charge carrier density measured using capacitance–voltage measurements[37] remains similar (Figure S11, Supporting Information). Following the discussion in Section 2.3.1, this trend indicates that the increase in the PL yield (Y_{PL}) is due to an increase in charge carrier lifetime (τ_n), according to $Y_{PL} \propto \tau_n B p_0$, where B and p_0 are the radiative recombination coefficient and the charge-carrier (doping) density, respectively.[5,38] Indeed, the normalized TRPL data in Figure 3b show an increase in the PL decay time as the Cu/[Cd+Sn] ratio decreases.

Recently, neutron diffraction measurements revealed an increase in density of V_{Cu} as the Cu/[Zn+Sn] ratio decreases in $Cu_2ZnSnSe_4$.[26] Although such detailed structural studies are not yet available for Cu_2CdSnS_4, we expect similar qualitative trends in Cu_2CdSnS_4. As discussed in Section 2.2.4, experimentally decreasing the Cu/[Cd+Sn] ratio can be modeled in DFT calculations as the addition of V_{Cu} in the Cu_2CdSnS_4 structure. The increasing PL decay time and PL yield with lower Cu content agrees with the DFT prediction of $2Cu_{Cd}+Sn_{Cd}$ deep-trap suppression in the presence of V_{Cu} in Cu_2CdSnS_4 (Figure 2b). Thus, based on the consistent improvement in the PL decay time and steady-state PL yield, we infer that the Cu/[Cd+Sn] ratio influences the minority carrier lifetime, primarily due to the destabilizing effect of V_{Cu} on the deep $2Cu_{Cd}+Sn_{Cd}$ defects.

2.4. Optoelectronic Properties

We performed external quantum efficiency (EQE) measurements (**Figure 4**a) to study the effect of Cd on the bandgap (Figure 4b), bandgap fluctuations (Figure 4b), and the Urbach energy (Figure 4c). We also measured the current–voltage (*IV*) characteristics under AM1.5 radiation to study the photovoltaic parameters; we present the *IV* curves for the best-performing devices in Figure 4d and statistical data in Figure S12 in the Supporting Information.

2.4.1. Bandgap and Bandgap Fluctuations

In the wavelength range of ≈700–850 nm for Cu_2ZnSnS_4 and ≈800–900 nm for Cu_2CdSnS_4, the drop in EQE is primarily due to the bandgap onset. This drop is steeper for Cu_2CdSnS_4 (0.86) as compared to Cu_2ZnSnS_4 (Figure 4a). Changing the Cu content in Cu_2CdSnS_4 influences this slope. To make the analysis

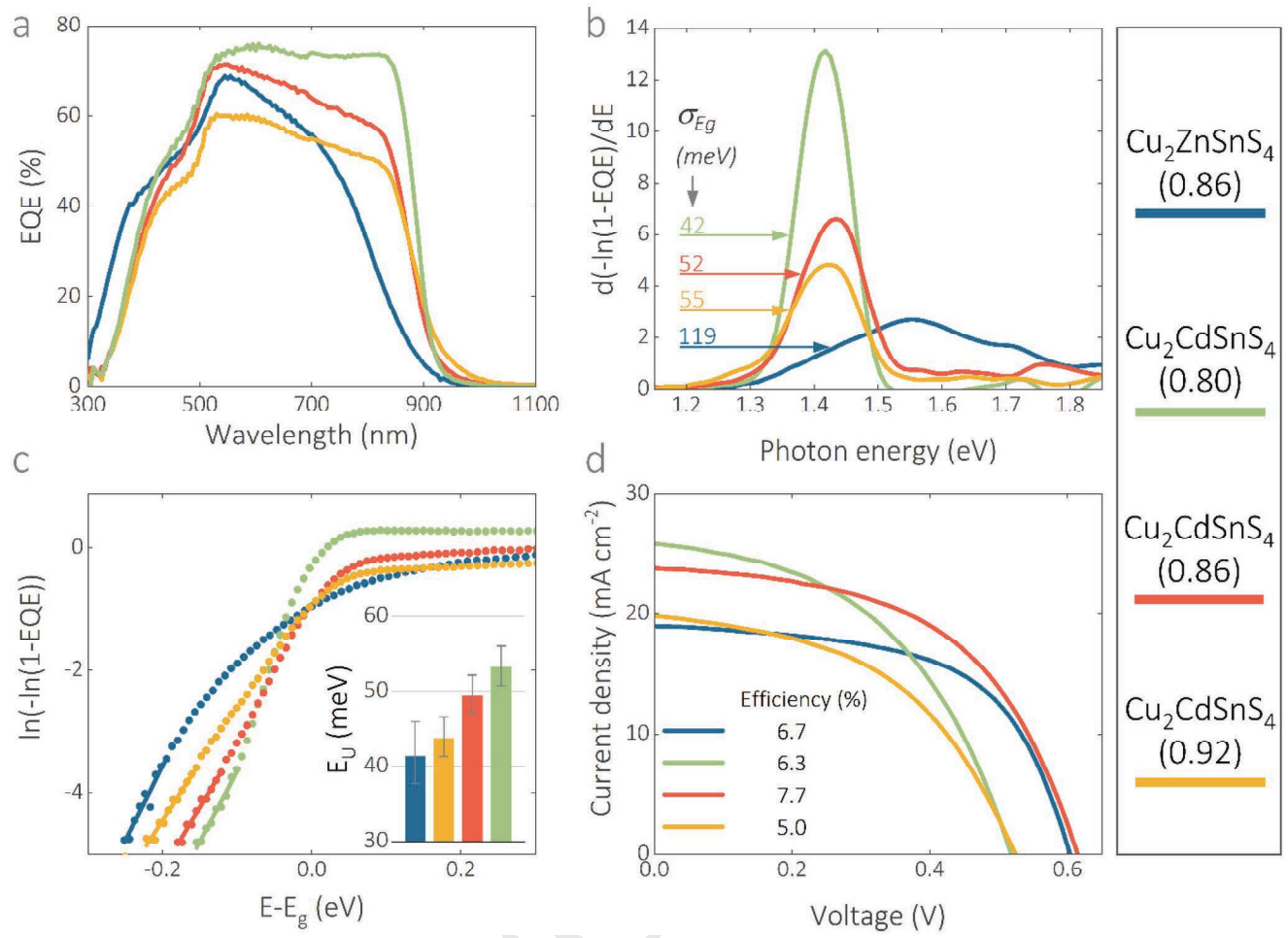

Figure 4. a) External quantum efficiency (EQE), b) standard deviation σ_{Eg} of the Gaussian distribution of bandgap energies, c) Urbach energy, and d) current–voltage characteristics for Cu_2ZnSnS_4 (Cu/[Zn+Sn] = 0.86) and Cu_2CdSnS_4 (Cu/[Cd+Sn] = 0.80, 0.86, and 0.92).

quantitative, we analyze the derivative of the absorption spectrum extracted from the EQE, following the methods described by Mattheis et al.[39,40] The width parameter of a Gaussian fit to the derivative of the absorption spectrum (that is, the peak in d(–ln(1 – EQE))/dE vs E) has been associated with the degree of bandgap fluctuations; the bandgap then is identified from the peak position in this derivative plot (Figure 4b). Consistent with other studies,[41] we find that the bandgap of Cu_2ZnSnS_4 (1.55 eV) decreases with Cd substitution with values of 1.42–1.43 eV for Cu_2CdSnS_4.

The standard deviation (σ_{Eg}) of the bandgap fluctuation also narrows with Cd substitution, with widths of 119 meV for Cu_2ZnSnS_4(0.86) versus 52 meV for Cu_2CdSnS_4(0.86). Prior studies have attributed the bandgap fluctuations to defects resulting from disorder in the Cu-Zn sub-lattice.[14] However, we predict that the formation energy of the Cu_{Zn}+Zn_{Cu} defects in Cu_2ZnSnS_4 is similar to that of Cu_{Cd}+Cd_{Cu} in Cu_2CdSnS_4 (see Section 2.2.2). Moreover, the band-edge narrowing due to the Cu/Zn and Cu/Cd disorder is reported to be small, with band-edge shift <0.1 eV.[11,12] Hence, we infer that the likely reason for smaller bandgap fluctuations in Cu_2CdSnS_4 as compared to Cu_2ZnSnS_4 is the suppression of the $2Cu_{Cd}$+Sn_{Cd} clusters as compared to $2Cu_{Zn}$+Sn_{Zn}, which cause a significant conduction band downshift.[11,12] Recently, using absorbance and PL measurements on $Cu_2ZnSn(S,Se)_4$, Siebentritt and coworkers reached a similar conclusion—that the Cu/Zn disorder is not directly responsible for band-edge fluctuations and that $2Cu_{Zn}$+Sn_{Zn} is more likely to contribute towards band-edge fluctuations.[13] The role of $2Cu_{Zn}$+Sn_{Zn} and $2Cu_{Cd}$+Sn_{Cd} in promoting bandgap fluctuations is also supported by the observation that decreasing the copper content (Cu/[Cd+Sn] ratio) in Cu_2CdSnS_4 from 0.86 to 0.80, which increases the formation energy for $2Cu_{Cd}$+Sn_{Cd} (see Section 2.2.4), decreases the bandgap fluctuations in Cu_2CdSnS_4 from 52 to 42 meV.

Comparison of the d(–ln(1 – EQE))/dE versus E plot for Cu/[Cd+Sn] = 0.80 with the data extracted from currently published record Cu_2ZnSnS_4,[42] $Cu_2ZnSn(S,Se)_4$,[3] and $Cu_2ZnSnSe_4$[43] based devices (Figure S13a, Supporting Information) shows that Cu_2CdSnS_4 has smaller bandgap fluctuations than the record devices. Furthermore, comparing the corresponding data from various publications (Figure S13b,c, Supporting Information),[3,7,9,42–44] which include high-efficiency devices for Ag-, Cd-, Ge-, and Ba-alloyed absorbers, only Ba-alloyed absorbers have smaller bandgap fluctuations than Cu_2CdSnS_4 (Figure S13c, Supporting Information). Interestingly, similar to Cd, Ba also replaces Zn in Cu_2ZnSnS_4. Thus, the +2 cation

and its role in destabilizing antisites seem to influence bandgap fluctuations significantly. However, the substitution of Zn with Cd and Ba also changes the crystal structure from kesterite to stannite and trigonal, respectively. Hence, further studies that decouple the effect of cation substitution on the +2 site with the structural changes associated with it may help understand the nature of bandgap fluctuations in kesterites.

2.4.2. Urbach Energy

In the long wavelength region (>900 nm) the exponential decay in EQE is due to band tails, which can be quantified with the Urbach energy parameter, E_U in the equation for exponential absorption edge: $\alpha(E) = \alpha_0 e^{E/E_U}$ (Figure 4c). Specifically, we calculate the Urbach energy from the inverse slope of the linear portion in the sub-bandgap region of the plot between ln(–ln(1 − EQE)) and $E - E_g$.[45] We extract an Urbach energy of ≈40–55 meV for all of the samples. Although the E_U values are slightly overestimated due to inefficient charge-carrier collection at long wavelengths (see Section 2.4.3), the values measured here are consistent with those extracted from photothermal deflection spectroscopy measurements by Huang et al., where an E_U of 53 meV was measured for both Cu_2ZnSnS_4 and Cu_2CdSnS_4.[36] Due to significant ambiguity in the selection of the linear region of the ln(–ln(1 − EQE)) plot and the large standard deviation within the linear fit, conclusive trends cannot be extracted from the E_U values.

2.4.3. Current–Voltage Characteristics

At the same Cu/[Zn+Sn] and Cu/[Cd+Sn] ratio, the substitution of Zn with Cd improves the PCE, open-circuit voltage (V_{OC}), and short-circuit current (J_{SC}) (Figure 4d). **Table 1** lists the relevant photovoltaic parameters for Cu_2ZnSnS_4(0.86) and Cu_2CdSnS_4(0.86). The bandgap decreases when Zn is substituted with Cd, and hence we use the bandgap-unbiased metrics,[46] $V_{OC}/V_{OC,SQ}$ and $J_{SC}/J_{SC,SQ}$ (where $J_{SC,SQ}$ and $V_{OC,SQ}$ are the Shockley–Queisser limits for J_{SC} and V_{OC}, respectively), to compare the performance of Cu_2ZnSnS_4 and Cu_2CdSnS_4.

Open-Circuit Voltage: The $V_{OC}/V_{OC,SQ}$ improved from 47.3% for Cu_2ZnSnS_4(0.86) to 52.3% for Cu_2CdSnS_4(0.86). This improvement has two origins: i) the smaller bandgap fluctuations in Cu_2CdSnS_4(0.86) compared to Cu_2ZnSnS_4(0.86) and ii) the longer PL decay time for Cu_2CdSnS_4(0.86) compared to Cu_2ZnSnS_4(0.86).

The reduction of V_{OC} in the presence of bandgap fluctuations, σ_{Eg}, can be estimated using $\sigma_{Eg}^2/2k_bTq$.[39] Based on the bandgap fluctuation values extracted above, the σ_{Eg}-related V_{OC} loss is estimated to be 51 mV for Cu_2CdSnS_4(0.86) and 283 mV for Cu_2ZnSnS_4. These values for the V_{OC} loss are slightly overestimated, due to inefficient charge-carrier collection at longer wavelengths in the EQE data, especially for Cu_2ZnSnS_4. Regardless, the smaller bandgap fluctuations should improve the V_{OC} in Cu_2CdSnS_4(0.86) as compared to Cu_2ZnSnS_4(0.86). However, although the reduction of the V_{OC} loss with respect to the radiative limit observed here (i.e., $[V_{OC,SQ} - V_{OC}]_{CZTS} - [V_{OC,SQ} - V_{OC}]_{CCdTS} = 130$ mV) does not improve as much as the σ_{Eg}-analysis would suggest (i.e., $\sigma_{Eg,CZTS} - \sigma_{Eg,CCdTS} = 232$ mV), the lower σ_{Eg}-related V_{OC} loss is promising for further development of Cu_2CdSnS_4-based photovoltaics and optoelectronics.

The improvement in $V_{OC}/V_{OC,SQ}$ for Cu_2CdSnS_4 (0.86) as compared to Cu_2ZnSnS_4(0.86) also can be attributed to the increased PL decay time. The V_{OC} increases with increasing charge-carrier lifetime according to $V_{OC} = (kT/q)\ln[(\Delta n(N_A + \Delta p)/n_i^2) + 1]$, where Δn is the excess photogenerated minority carrier density, which is proportional to the minority carrier lifetime, which in turn is proportional to the PL decay time.[5,47] The improved optoelectronic properties for Cu/[Cd+Sn] = 0.80 thus would be expected to result in a higher V_{OC}. However, we do not observe this. Although the steady-state PL yield (Figure 3c) and PL decay time (Figure 3b) for Cu/[Cd+Sn] = 0.80 are larger than those for Cu/[Cd+Sn] = 0.86, the measured V_{OC} for Cu_2CdSnS_4(0.86) is larger than that for Cu_2CdSnS_4(0.80) (Figure 4d). This apparent contradiction suggests that aside from the small charge-carrier lifetime of Cu_2ZnSnS_4 further limits exist to the V_{OC}. One possible reason for the lack of a consistent correlation between the PL decay time (and steady-state PL yield) and V_{OC} could be the presence of severe nonidealities at the heterointerface.

The V_{OC} for a solar cell under illumination is related to the quasi-Fermi level splitting and interface energetics, and in cases of severe interface recombination also may be limited by the built-in voltage (or band bending at the heterojunction). Hence, to understand the trend in the built-in voltage, we performed a Mott–Schottky analysis, although such an analysis is strictly possible only for homogeneous doping profiles and thus in the case of nonideal devices could give only rough indications of the trend (Figure S14, Supporting Information). The built-in voltage deduced from the voltage intercept is maximum for Cu/[Cd+Sn] = 0.86 at all the AC frequencies used here, consistent with the higher V_{OC} observed for this ratio. Hence, the trend in V_{OC} (higher for Cu/[Cd+Sn] = 0.86 as compared to Cu/[Cd+Sn] = 0.80 and 0.92) in these devices correlates not to the trend in PL decay time and PL yield (higher for Cu/[Cd+Sn] = 0.80 as compared to Cu/[Cd+Sn] = 0.86 and 0.92) but with the built-in voltage. Moreover, for the case of partial substitution of Zn with Cd, we highlighted in our previous work that the energy level of the acceptor defects in the bandgap affects the V_{OC} more significantly than the PL decay time.[22] These results indicate that, apart from the short charge-carrier lifetime, other factors such as interface

Table 1. Photovoltaic parameters for Cu_2ZnSnS_4 and Cu_2CdSnS_4 at Cu/[Zn+Sn] = Cu/[Cd+Sn] = 0.86.

	Efficiency [%]	J_{SC} [mA cm^{-2}]	V_{OC} [V]	FF [%]	E_g [eV]	σ_{Eg} [eV]	$J_{SC,SQ}$ [mA cm^{-2}]	$V_{OC,SQ}$ [v]	$J_{SC}/J_{SC,SQ}$ [%]	$V_{OC}/V_{OC,SQ}$ [%]
Cu_2ZnSnS_4	6.7	19.0	0.604	58.3	1.55	0.119	27.4	1.276	69.3	47.3
Cu_2CdSnS_4	7.7	23.8	0.615	52.6	1.42	0.052	32.1	1.156	74.1	53.2

nonidealities, built-in voltages, and depth of acceptor defects, also may limit the V_{OC}.

Short-Circuit Current: $J_{SC}/J_{SC,SQ}$ improves from 69.4% for Cu_2ZnSnS_4(0.86) to 74.1% for Cu_2CdSnS_4(0.86). Based on the EQE data, this improvement is primarily due to the enhanced charge-carrier collection in Cu_2CdSnS_4 (note that the small improvement in the EQE for Cu_2ZnSnS_4 in the wavelength range 300–400 nm is due to the increased absorption in the transparent conducting oxide (TCO) layer upon postannealing). For wavelengths longer than those that are absorbed in CdS or TCO layers and shorter than the absorption edge (that is, ≈550–750 nm for Cu_2ZnSnS_4 and ≈550–825 nm for Cu_2CdSnS_4), the slope of the EQE graph depends on the drift and diffusion of photogenerated charge carriers in the bulk absorber. Since the reflectance (Figure S9, Supporting Information) in this region is similar for Cu_2ZnSnS_4 and Cu_2CdSnS_4, a steeper slope in this region suggests inefficient charge-carrier collection. It is clear that the slope in this region is steeper for Cu_2ZnSnS_4(0.86) than for Cu_2CdSnS_4(0.86), which suggests that inefficient charge-carrier collection contributes to the lower $J_{SC}/J_{SC,SQ}$ for Cu_2ZnSnS_4. The drift of photogenerated charge carriers depends on the degree of band bending and their diffusion depends on the minority carrier lifetime. The diffusion length *(L)* of charge carriers is given by $L = \sqrt{D \times \tau}$, where D is the carrier diffusivity, and τ is the carrier lifetime. The increased diffusion length allows charge carriers that are photogenerated deep in the absorber film to diffuse to their respective contacts before recombination. The PL and TRPL results qualitatively suggest a larger charge-carrier lifetime for Cu_2CdSnS_4(0.86) than for Cu_2ZnSnS_4(0.86). This in turn should produce a larger carrier diffusion length for Cu_2CdSnS_4, and consequently, better carrier collection. This effect of a larger diffusion length leading to better carrier collection also is observed for Cu_2CdSnS_4(0.80), which shows the longest PL decay time and the best carrier collection characteristics in the EQE. However, Cu_2CdSnS_4(0.92) does not follow this trend and the entire EQE curve shifts to lower values, which could be due to interface recombination.

We propose that the better charge-carrier collection for Cu_2CdSnS_4(0.86) as compared to Cu_2ZnSnS_4(0.86) is primarily due to the suppression of the deep $2Cu_{Zn}+Sn_{Zn}$ defect. Hence, further improvements in the J_{SC} for Cu_2ZnSnS_4 should focus on the improvement of minority carrier lifetime. This is especially important for sulfide kesterites, since DFT calculations predict that the energy level of the electron traps is deeper and the formation energy of the isolated Sn_{Zn} is lower in sulfide kesterites than in selenide kesterites.[12] This might also be one of the reasons for the decreasing trend in the $J_{SC}/J_{SC,SQ}$ values for the record kesterite devices with increasing S/Se ratio: the 11.6% $Cu_2ZnSnSe_4$,[43] 12.6% $Cu_2ZnSn(S,Se)_4$,[3] and 11.01% Cu_2ZnSnS_4[42] devices achieved $J_{SC}/J_{SC,SQ}$ equal to 84.2%, 81.6%, and 74.9%, respectively.

Champion Device: Finally, we empirically tuned the TCO deposition and precursor spin coating conditions (see methods for details) to optimize the solar cell fabrication for Cu_2CdSnS_4 (Cu/[Cd+Sn] = 0.86) and obtained 7.96% efficiency (7.85% total area efficiency) device (**Figure 5**), which is the highest efficiency among fully cation substituted absorbers based on $Cu_2ZnSn(S,Se)_4$ (**Table 2**) .

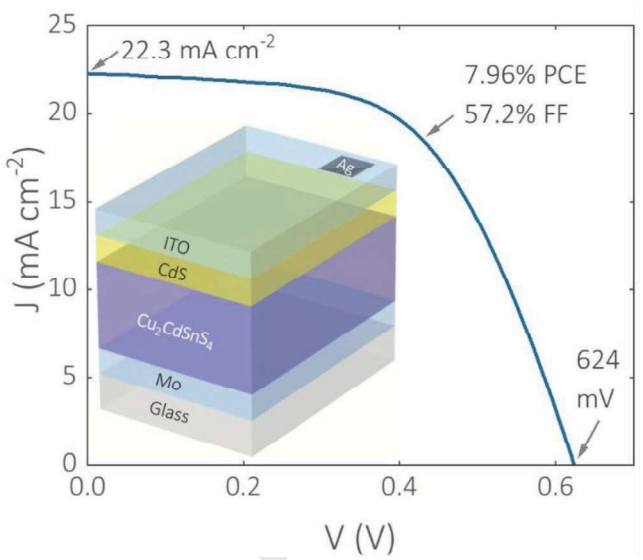

Figure 5. Current–voltage characteristics for the champion Cu_2CdSnS_4 device under simulated AM1.5 radiation.

3. Conclusion

The consistently observed drawbacks in kesterite solar cells are related to the defect characteristics of Cu_2ZnSnS_4. Using experiments and theoretical calculations, we provided insights into the causes of these drawbacks. Using comparisons in defect formation energies, photoluminescence characteristics, and device performance data, we concluded that deep-defect-level-inducing $2Cu_{Zn}+Sn_{Zn}$ clusters may be the main cause of nonradiative recombination in kesterites, and that cation substitution may offer a promising way to alter the formation energy of this defect cluster. Further, we showed that bandgap fluctuations, which can arise out of either composition fluctuations or disorder-inducing antisites, can be moderated by cation substitution with Cd. By varying the Cu/[Cd+Sn] ratio in Cu_2CdSnS_4, we highlighted the deleterious role of the $2Cu_{Zn}+Sn_{Zn}$ defect cluster and observed that bandgap fluctuations are influenced by the Cu/[Cd+Sn] ratio. We predict from theory that synthesis under Cu-poor conditions destabilizes this defect cluster through its interactions with Cu vacancies, suggesting such conditions will help produce optimal properties. Importantly, we found that although the PL decay time improves with decreasing copper content, the V_{OC} in Cu_2CdSnS_4 devices with varying Cu/[Cd+Sn] ratio does not follow the improved PL decay time, which may be due to severe nonidealities at the heterointerface. Based on these results and analyses on high

Table 2. Record efficiencies for fully cation substituted absorbers based on $Cu_2ZnSn(S,Se)_4$.

Absorber	Efficiency [%]	Absorber deposition method
Cu_2**Cd**SnS_4	7.96 (this work)	Spin-coating
Cu_2Zn**Ge**Se_4	7.6[53]	Sputtering and e-beam evaporation
Ag$_2ZnSnSe_4$	5.2[54]	Coevaporation
Cu_2**Ba**$Sn(S,Se)_4$	5.2[9]	Cosputtering
Cu_2**Fe**SnS_4	2.9[55]	SILAR

efficiency Cu_2CdSnS_4, we show that cation substitution not only can be used to improve the performance of kesterites but also to systematically study their performance-limiting factors. Finally, the suppressed deep defects and bandgap fluctuations lead to a promising 7.96% efficient Cu_2CdSnS_4, which could be further improved with device optimization.

4. Experimental Section

DFT Calculations: All defect calculations in kesterite-Cu_2ZnSnS_4, stannite-Cu_2ZnSnS_4, and stannite-Cu_2CdSnS_4 were performed using spin-polarized DFT,[48] as implemented in the Vienna ab initio simulation package.[49] Only neutral defects were considered in the calculations, i.e., all the electrons of all species that are removed (added) for the creation of a defect in an otherwise pristine structure were removed (added). The all-electron, frozen-core, projector-augmented-wave (PAW) theory[50] was employed with standard PAW projectors representing the screened nuclei. A kinetic energy cut-off of 520 eV was used for the plane wave basis. The one-electron orbitals are sampled on a well-converged Γ-point-centered $3 \times 3 \times 1$ *k*-point mesh that converges total energies to within 0.05 meV per atom on a $2 \times 2 \times 2$ supercell of the conventional kesterite/stannite-Cu_2ZnSnS_4 and stannite-Cu_2CdSnS_4. Consistent with earlier work,[15] the strongly constrained and appropriately normed functional[51] was used to describe the electronic exchange-correlation interactions. Also, the framework to estimate the chemical potentials needed for calculating the various defect formation energies is detailed in a previous publication.[15]

Thin-Film Deposition: The thin-films and devices were fabricated using the same methods outlined in the previous work.[22] In brief, the spin-coating solutions were made by dissolving an appropriate quantity of copper acetate hydrate, zinc acetate dihydrate, cadmium acetate dihydrate, tin chloride dihydrate, and thiourea in 2-methoxyethanol. This solution was spin coated on Mo-glass substrates at ≈4000 rpm and then annealed at 280 °C for 2 min to vaporize the excess solvent. This spin-coating-annealing step was repeated 13 times. For the champion device in Figure 5, the spin coating was performed at 3900 rpm and repeated 12 times. Then, the Cu_2ZnSnS_4 films were sulfurized at 600 °C and the Cu_2CdSnS_4 films were sulfurized at 580 °C in a two-zone tube furnace.

Device Fabrication: Devices were fabricated by depositing a thin layer of CdS using chemical bath deposition, followed by deposition of ITO using DC magnetron sputtering (50 W power for 55 min; for the champion device in Figure 5, 75 W power for 60 min). Cu_2ZnSnS_4 devices were postannealed at 300 °C for 10 min in Ar atmosphere. A silver paste was used to print the top electrode and devices were delineated using mechanical scribing (with area 0.16 cm^2). Active area efficiencies (unless mentioned otherwise) were reported and no antireflection coating was used for any of the devices.

Thin-Film Characterization: XRD measurements were performed using a "Bruker D8 Advance" system, using Cu-K_α radiation (40 mA, 40 kV) in the grazing-incidence configuration with a grazing angle of 4°, and XRD simulations were performed using VESTA.[52] TRPL measurements on absorber films were performed using the system described by Hages et al.,[5] with a 660 nm pulsed-laser source and an excitation spot diameter of 30 µm. Time resolution was achieved using time-correlated single-photon counting with an InGaAs detector. Prior to the TRPL measurements, the samples were etched in a 1 M HCl solution for 1 min.[5] PL and Raman measurements on thin films were performed in a back-scattering configuration with a LabRam HR800-UV and T64000 Horiba-Jobin Yvon spectrometers. It was ensured that there were no thermal effects due to the laser excitation by monitoring the Raman peak positions and intensity as a function the incident laser power. Raman measurements were performed at three different points on each sample to confirm sample homogeneity.

Device Characterization: Current–voltage characteristics were measured using a Keithley 2612A SMU. A Xe-lamp-based VS-0852 solar simulator was used to simulate AM1.5 conditions using a certified standard Si cell as a reference. External quantum efficiencies of the devices were measured using a Bentham PVE300 system and a certified standard Si cell was used for calibration. PL on devices was initiated by a 660 nm diode laser and collected using a ½-m grating monochromator coupled with a liquid-nitrogen-cooled InGaAs diode array. Impedance spectroscopy measurements were performed using an Autolab PGSTAT302N, and the devices were kept in the dark for 2 h prior to the impedance measurements.

Supporting Information

Supporting Information is available from the Wiley Online Library or from the author.

Acknowledgements

L.H.W. and S.H. acknowledge the funding support from the CREATE Programme under the Campus for Research Excellence and Technological Enterprise (CREATE), which was supported by the National Research Foundation, Prime Minister's Office, Singapore; and the Ministry of Education (MOE) Tier 2 Project (MOE2016-T2-1-030). E.A.C. acknowledges support from U.S. Department of Energy, Office of Science, Basic Energy Sciences under Award No. DE-SC0002120, and from Princeton University for computing resources. V.I.-R. acknowledges support by the H2020 Programme under the project INFINITE-CELL (H2020-MSCA-RISE-2017-777968), by the Spanish Ministry of Science, Innovation and Universities under the IGNITE (ENE2017-87671-C3-1-R), and by the European Regional Development Funds (ERDF, FEDER Programa Competitivitat de Catalunya 2007–2013). V.I.-R. belongs to the SEMS (Solar Energy Materials and Systems) Consolidated Research Group of the "Generalitat de Catalunya" (Ref. 2017 SGR 862). T.U. and S.L. acknowledge support by the project INFINITE-CELL (H2020-MSCA-RISE-2017-777968).

Conflict of Interest

The authors declare no conflict of interest.

Keywords

antisite defects, bandgap fluctuations, CZTS, DFT, kesterite

Received: August 1, 2019
Revised: September 19, 2019
Published online:

[1] a) A. Chirilă, P. Reinhard, F. Pianezzi, P. Bloesch, A. R. Uhl, C. Fella, L. Kranz, D. Keller, C. Gretener, H. Hagendorfer, *Nat. Mater.* **2013**, *12*, 1107; b) J. Major, R. Treharne, L. Phillips, K. Durose, *Nature* **2014**, *511*, 334.

[2] M. A. Green, Y. Hishikawa, E. D. Dunlop, D. H. Levi, J. Hohl-Ebinger, M. Yoshita, A. W. Y. Ho-Baillie, *Prog. Photovoltaics* **2019**, *27*, 3.

[3] W. Wang, M. T. Winkler, O. Gunawan, T. Gokmen, T. K. Todorov, Y. Zhu, D. B. Mitzi, *Adv. Energy Mater.* **2014**, *4*, 1301465.

[4] a) A. Polizzotti, I. L. Repins, R. Noufi, S.-H. Wei, D. B. Mitzi, *Energy Environ. Sci.* **2013**, *6*, 3171; b) X. Liu, Y. Feng, H. Cui, F. Liu, X. Hao, G. Conibeer, D. B. Mitzi, M. Green, *Prog. Photovoltaics* **2016**, *24*, 879; c) D. B. Mitzi, O. Gunawan, T. K. Todorov, D. A. Barkhouse,

Philos. Trans. R. Soc., A **2013**, *371*, 20110432; d) S. Bourdais, C. Choné, B. Delatouche, A. Jacob, G. Larramona, C. Moisan, A. Lafond, F. Donatini, G. Rey, S. Siebentritt, A. Walsh, G. Dennler, *Adv. Energy Mater.* **2016**, *6*, 1502276.

[5] C. J. Hages, A. Redinger, S. Levcenko, H. Hempel, M. J. Koeper, R. Agrawal, D. Greiner, C. A. Kaufmann, T. Unold, *Adv. Energy Mater.* **2017**, *7*, 1700167.

[6] D. Shin, B. Saparov, D. B. Mitzi, *Adv. Energy Mater.* **2017**, *7*, 1602366.

[7] S. Kim, K. M. Kim, H. Tampo, H. Shibata, S. Niki, *Appl. Phys. Express* **2016**, *9*, 102301.

[8] K. Yu, E. A. Carter, *Chem. Mater.* **2015**, *27*, 2920.

[9] D. Shin, T. Zhu, X. Huang, O. Gunawan, V. Blum, D. B. Mitzi, *Adv. Mater.* **2017**, *29*, 1606945.

[10] K. Yu, E. A. Carter, *Chem. Mater.* **2016**, *28*, 864.

[11] Z.-K. Yuan, S. Chen, H. Xiang, X.-G. Gong, A. Walsh, J.-S. Park, I. Repins, S.-H. Wei, *Adv. Funct. Mater.* **2015**, *25*, 6733.

[12] S. Chen, A. Walsh, X. G. Gong, S. H. Wei, *Adv. Mater.* **2013**, *25*, 1522.

[13] G. Rey, G. Larramona, S. Bourdais, C. Choné, B. Delatouche, A. Jacob, G. Dennler, S. Siebentritt, *Sol. Energy Mater. Sol. Cells* **2018**, *179*, 142.

[14] J. Bleuse, F. Ducroquet, H. Mariette, *J. Electron. Mater.* **2018**, *47*, 4282.

[15] G. Sai Gautam, T. P. Senftle, E. A. Carter, *Chem. Mater.* **2018**, *30*, 4543.

[16] S. Chen, X. G. Gong, A. Walsh, S.-H. Wei, *Appl. Phys. Lett.* **2010**, *96*, 021902.

[17] S. Chen, J.-H. Yang, X. G. Gong, A. Walsh, S.-H. Wei, *Phys. Rev. B* **2010**, *81*, 245204.

[18] S. Chen, L.-W. Wang, A. Walsh, X. G. Gong, S.-H. Wei, *Appl. Phys. Lett.* **2012**, *101*, 223901.

[19] Y. S. Yee, B. Magyari-Köpe, Y. Nishi, S. F. Bent, B. M. Clemens, *Phys. Rev. B* **2015**, *92*, 195201.

[20] J. Li, D. Wang, X. Li, Y. Zeng, Y. Zhang, *Adv. Sci.* **2018**, *5*, 1700744.

[21] X. Li, Z. Hou, S. Gao, Y. Zeng, J. Ao, Z. Zhou, B. Da, W. Liu, Y. Sun, Y. Zhang, *Sol. RRL* **2018**, *2*, 1800198.

[22] S. H. Hadke, S. Levcenko, S. Lie, C. J. Hages, J. A. Márquez, T. Unold, L. H. Wong, *Adv. Energy Mater.* **2018**, *8*, 1802540.

[23] Z. Su, J. M. R. Tan, X. Li, X. Zeng, S. K. Batabyal, L. H. Wong, *Adv. Energy Mater.* **2015**, *5*, 1500682.

[24] R. D. Shannon, *Acta Crystallogr. A* **1976**, *32*, 751.

[25] T. Gershon, D. Bishop, P. Antunez, S. Singh, K. W. Brew, Y. S. Lee, O. Gunawan, T. Gokmen, T. Todorov, R. Haight, *Curr. Opin. Green Sustainable Chem.* **2017**, *4*, 29.

[26] G. Gurieva, L. E. Valle Rios, A. Franz, P. Whitfield, S. Schorr, *J. Appl. Phys.* **2018**, *123*, 161519.

[27] J. H. Hubbell, W. J. Veigele, E. A. Briggs, R. T. Brown, D. T. Cromer, R. J. Howerton, *J. Phys. Chem. Ref. Data* **1975**, *4*, 471.

[28] S. Schorr, *Sol. Energy Mater. Sol. Cells* **2011**, *95*, 1482.

[29] T. Washio, H. Nozaki, T. Fukano, T. Motohiro, K. Jimbo, H. Katagiri, *J. Appl. Phys.* **2011**, *110*, 074511.

[30] a) M. Dimitrievska, A. Fairbrother, X. Fontané, T. Jawhari, V. Izquierdo-Roca, E. Saucedo, A. Pérez-Rodríguez, *Appl. Phys. Lett.* **2014**, *104*, 021901; b) T. Gürel, C. Sevik, T. Çağın, *Phys. Rev. B* **2011**, *84*, 205201.

[31] a) C. Freysoldt, B. Grabowski, T. Hickel, J. Neugebauer, G. Kresse, A. Janotti, C. G. Van de Walle, *Rev. Mod. Phys.* **2014**, *86*, 253; b) G. Sai Gautam, T. P. Senftle, N. Alidoust, E. A. Carter, *J. Phys. Chem. C* **2018**, *122*, 27107.

[32] P. Canepa, G. Sai Gautam, D. Broberg, S.-H. Bo, G. Ceder, *Chem. Mater.* **2017**, *29*, 9657.

[33] P. Zawadzki, A. Zakutayev, S. Lany, *Phys. Rev. Appl.* **2015**, *3*, 034007.

[34] S. Levcenko, J. Just, A. Redinger, G. Larramona, S. Bourdais, G. Dennler, A. Jacob, T. Unold, *Phys. Rev. Appl.* **2016**, *5*, 024004.

[35] M. Pilvet, M. Kauk-Kuusik, M. Grossberg, T. Raadik, V. Mikli, R. Traksmaa, J. Raudoja, K. Timmo, J. Krustok, *J. Alloys Compd.* **2017**, *723*, 820.

[36] J. Huang, C. Yan, K. Sun, F. Liu, M. Green, X. Hao, *2018 IEEE 7th World Conf. Photovoltaic Energy Convers. (WCPEC) (Jt. Conf. 45th IEEE PVSC, 28th PVSEC 34th EU PVSEC)* **2018**, p. 0827. Q14

[37] T. Eisenbarth, T. Unold, R. Caballero, C. A. Kaufmann, H.-W. Schock, *J. Appl. Phys.* **2010**, *107*, 034509.

[38] T. Unold, L Gutay, in *Advanced Characterization Techniques for Thin Film Solar Cells* (Eds: D. Abou-Ras, T. Kirchartz, U. Rau), John Wiley & Sons, **2016**, Ch. 7. Q15

[39] J. Mattheis, U. Rau, J. H. Werner, *J. Appl. Phys.* **2007**, *101*, 113519.

[40] U. Rau, B. Blank, T. C. M. Müller, T. Kirchartz, *Phys. Rev. Appl.* **2017**, *7*, 044016.

[41] a) S. Levcenko, C. J. Hages, S. Hadke, H. Stange, R. Mainz, L. H. Wong, R. Agrawal, T. Unold, *2018 IEEE 7th World Conf. Photovoltaic Energy Convers. (WCPEC) (Jt. Conf. 45th IEEE PVSC, 28th PVSEC 34th EU PVSEC)* **2018**, p. 1918; b) Y. F. Tay, H. Kaneko, S. Y. Chiam, S. Lie, Q. Zheng, B. Wu, S. S. Hadke, Z. Su, P. S. Bassi, D. Bishop, T. C. Sum, T. Minegishi, J. Barber, K. Domen, L. H. Wong, *Joule* **2018**, *2*, 537. Q16

[42] C. Yan, J. Huang, K. Sun, S. Johnston, Y. Zhang, H. Sun, A. Pu, M. He, F. Liu, K. Eder, L. Yang, J. M. Cairney, N. J. Ekins-Daukes, Z. Hameiri, J. A. Stride, S. Chen, M. A. Green, X. Hao, *Nat. Energy* **2018**, *3*, 764.

[43] Y. S. Lee, T. Gershon, O. Gunawan, T. K. Todorov, T. Gokmen, Y. Virgus, S. Guha, *Adv. Energy Mater.* **2015**, *5*, 1401372.

[44] a) C. Yan, K. Sun, J. Huang, S. Johnston, F. Liu, B. P. Veettil, K. Sun, A. Pu, F. Zhou, J. A. Stride, M. A. Green, X. Hao, *ACS Energy Lett.* **2017**, *2*, 930; b) Y. F. Qi, D. X. Kou, W. H. Zhou, Z. J. Zhou, Q. W. Tian, Y.-N. Meng, X.-S. Liu, Z. Du, S. X. Wu, *Energy Environ. Sci.* **2017**, *10*, 2401.

[45] C. J. Hages, M. J. Koeper, R. Agrawal, *Sol. Energy Mater. Sol. Cells* **2016**, *145*, 342.

[46] A. D. Collord, H. W. Hillhouse, *Chem. Mater.* **2016**, *28*, 2067.

[47] R. A. Sinton, A. Cuevas, *Appl. Phys. Lett.* **1996**, *69*, 2510.

[48] a) P. Hohenberg, W. Kohn, *Phys. Rev.* **1964**, *136*, B864; b) W. Kohn, L. J. Sham, *Phys. Rev.* **1965**, *140*, A1133.

[49] a) G. Kresse, J. Hafner, *Phys. Rev. B* **1993**, *47*, 558; b) G. Kresse, J. Furthmüller, *Phys. Rev. B* **1996**, *54*, 11169.

[50] G. Kresse, D. Joubert, *Phys. Rev. B* **1999**, *59*, 1758.

[51] J. Sun, A. Ruzsinszky, J. P. Perdew, *Phys. Rev. Lett.* **2015**, *115*, 036402.

[52] K. Momma, F. Izumi, *J. Appl. Crystallogr.* **2011**, *44*, 1272.

[53] L. Choubrac, G. Brammertz, N. Barreau, L. Arzel, S. Harel, M. Meuris, B. Vermang, *Phys. Status Solidi A* **2018**, *215*, 1800043.

[54] T. Gershon, K. Sardashti, O. Gunawan, R. Mankad, S. Singh, Y. S. Lee, J. A. Ott, A. Kummel, R. Haight, *Adv. Energy Mater.* **2016**, *6*, 1601182.

[55] S. Chatterjee, A. J. Pal, *Sol. Energy Mater. Sol. Cells* **2017**, *160*, 233.

